RSC Advances

PAPER

View Article Online
View Journal | View Issue

Check for updates

Cite this: *RSC Adv.*, 2026, **16**, 21359

Magnetic nanocrystalline cellulose-poly(methacrylic acid-*co*-acrylonitrile) composite: a versatile material for analytical and biological applications

Ali Khan,[ab] Hamayun Khan,*[a] Nasrullah Shah,*[c] Mahmoud Elodemi,[d] S. Tasqeeruddin,[e] Ajmal Khan*[fg] and Ahmed Al-Harrasi*[f]

Developing new materials for advanced analytical and biological applications is always a key target in the field of advanced materials. In the present study, a poly(methacrylic acid-*co*-acrylonitrile)-grafted-magnetic nanocrystalline cellulose composite [P(MAA-*co*-AN)-*g*-MNCC] was synthesized through a modified free-radical grafting co-polymerization method using cellulose recovered from waste paper. The synthesized composite was characterized *via* FTIR spectroscopy, SEM, EDX, and TGA, and its E_g, PZC, and surface area were determined. The as-synthesized P(MAA-*co*-AN)-*g*-MNCC was studied as an adsorbent for the removal of gallic acid (GA) from aqueous environments and as an antimicrobial and antioxidant agent. The influence of various experimental factors, including contact time, pH, temperature, and GA concentration, was investigated to optimize the adsorption process. The adsorption process follows pseudo-second-order kinetics and the Freundlich model with a spontaneous and exothermic nature. Similarly, the synthesized adsorbent maintained its excellent adsorption capacity when it was recycled and reused for four successive cycles in real samples. The synthesized P(MAA-*co*-AN)-*g*-MNCC also displayed good antioxidant and antibacterial activities against the tested pathogenic bacteria. The results indicated that the as-synthesized P(MAA-*co*-AN)-*g*-MNCC has the potential to be used as an effective advanced material for wastewater treatment and biomedical applications.

Received 19th January 2026
Accepted 8th April 2026

DOI: 10.1039/d6ra00474a

rsc.li/rsc-advances

Open Access Article. Published on 23 April 2026. Downloaded on 5/22/2026 8:14:12 PM.
This article is licensed under a Creative Commons Attribution-NonCommercial 3.0 Unported Licence.

1. Introduction

In the field of material science, chemistry, medicine, and biology, magnetic nanoparticles (MNPs) have significant importance due to their notable properties such as biocompatibility, non-toxicity, and cost-effective synthesis.[1,2] MNPs (magnetite Fe_3O_4 and maghemite γ-Fe_2O_3) show superparamagnetic properties and a high surface area-to-volume ratio, which endow them with the ability to carry, bind, and absorb various compounds like small drug molecules, proteins, DNA, RNA, and probes with remarkable efficiency.[3–11] Therefore, MNPs have attracted global attention, especially in the field of biomedical applications, such as cancer treatment, drug delivery, magnetic hyperthermia, and MRI.[12–17] However, their hydrophobic nature and the presence of van der Waals/electrostatic forces cause them to agglomerate, which restricts their applications.[18,19] Therefore, to avoid agglomeration, MNPs are coated with suitable inorganic/organic materials such as natural polysaccharides. To improve the chemical and thermal stability, biocompatibility, and biodegradability of synthesized MNPs, various polysaccharides, including chitosan, agar, carboxymethyl cellulose sodium, and carboxymethyl chitosan, are employed as stabilizers during their synthesis.[2,5,16,20]

Polysaccharide-based materials, especially the cellulose-based magnetic composites, are suitable for biomedical and environmental applications. However, the poor mechanical stability, high sensitivity to microbial attack, low sorption capacity, and uncontrolled water uptake of cellulose limit its application as a substrate for highly specific adsorbents.[21–23] In this case, its amorphous part can be removed to overcome these restrictions. For this purpose, nanocrystalline cellulose (NC) is produced using concentrated H_2SO_4, which has a highly

[a]*Department of Chemistry, Islamia College University, Peshawar 25120, Pakistan. E-mail: hamayun84@yahoo.com*
[b]*Department of Chemical Engineering, Bay Campus, Swansea University, Swansea, SA1 8EN, UK*
[c]*Department of Chemistry, Abdul Wali Khan University, Mardan 23200, Pakistan. E-mail: nasrullah@awkum.edu.pk*
[d]*Department of Pharmacology, Faculty of Medicine, University of Tabuk, Tabuk 71491, Saudi Arabia*
[e]*Department of Pharmacognosy, College of Pharmacy, King Khalid University, Asir 61441, Saudi Arabia*
[f]*Natural and Medical Sciences Research Center, University of Nizwa, PO Box 33, 616 Birkat Al Mauz, Nizwa, Oman. E-mail: ajmalchemist@yahoo.com; aharrasi@unizwa.edu.om*
[g]*Department of Chemical and Biological Engineering, College of Engineering, Korea University, Seoul 02841, Republic of Korea*

© 2026 The Author(s). Published by the Royal Society of Chemistry

Open Access Article. Published on 23 April 2026. Downloaded on 5/22/2026 8:14:12 PM. This article is licensed under a Creative Commons Attribution-NonCommercial 3.0 Unported Licence.

crystalline nature and excellent mechanical properties and offers maximum stability in solutions by preventing agglomeration. Graft copolymerization using vinyl monomers can further improve the dispersibility of NC in various solvents; furthermore, the addition of ionizable and hydrophobic functional groups to composite materials makes them pH-sensitive.[24]

Fe_3O_4 nanoparticles are incorporated into composite materials to impart magnetic responsiveness, enabling the rapid magnetic separation and efficient recovery of the adsorbent after analyte adsorption, thereby enhancing its reusability and practical applicability.[25,26] Cellulose acts as a hydroxyl-rich support that improves the grafting efficiency and structural stability while contributing to adsorption *via* hydrogen bonding interactions with gallic acid (GA).[27,28] Alternative hydroxyl-containing substrates may provide similar active sites; however, variations in functional group density and physicochemical properties could influence their adsorption performance and recyclability.

GA is a phenolic bioactive compound with a molecular mass of 170.12 mg L^{-1} and low water solubility.[29,30] GA has a wide range of applications, including anti-metastatic, antioxidant, anti-allergic, and anti-mutagenic agents. It is also utilized as a raw material in the manufacturing of imaging agents, dyes, inks, paints, foods, household chemicals, cosmetics, and pharmaceutical drugs.[31–36] A significant amount of GA is released into wastewater during the manufacturing process, which can have serious environmental consequences. The ecological impact of GA is concentration dependent. While it is generally considered safe and biodegradable at low concentrations, studies indicate that levels exceeding 200 mg L^{-1}, and particularly 500 mg L^{-1}, exhibit inhibitory effects on microbial populations and aquatic organisms due to its pro-oxidant potential and high chemical oxygen demand.[37,38]

For the isolation and degradation of GA from aqueous solution, different methods have been used, such as electrochemical oxidation, adsorption, ozonation treatment, UV/H_2O_2 treatment, biological degradation, and extraction.[29,36–40] However, these methods have benefits and drawbacks. Among them, the adsorption approach is the most popular and widely used for removing GA from aqueous environments due to its low cost and high efficiency. Various adsorbents, including biomass, resin, activated carbon, and magnetite nanoparticles, have been used to remove GA from the aqueous environment. Herein, we illustrate the synthesis of novel water-insoluble P(MAA-*co*-AN)-*g*-MNCC as a magnetically functionalized cross-linked polymer network. The pH sensitivity of the synthesized adsorbent was enhanced due to the presence of highly ionizable functionalities such as –COOH, and our goal was to utilize these functionalities for the removal of GA from an aqueous environment using the newly synthesized adsorbent under optimized conditions and determine its potential for biological applications. We previously reported the synthesis of chitosan-grafted terpolymer hydrogels for controlled drug delivery applications.[41] The synthetic procedure in this study differs fundamentally from our previous report. The current approach emphasizes a sustainable waste-to-material strategy by using waste-paper-derived nanocrystalline cellulose as the primary backbone. Furthermore, the integration of acrylonitrile (AN) provides a unique nitrogenous functionality, shifting the application from general drug delivery toward targeted removal and enhanced antibacterial activity.

2. Experimental

2.1. Materials

Analytical grade chemicals and reagents were used. Methacrylic acid (MAA), acrylonitrile (AN), potassium disulfate ($K_2S_2O_7$), and ethylene glycol dimethacrylate (EDGMA) were purchased from Sigma-Aldrich, USA. Iron(III) chloride hexahydrate ($FeCl_3 \cdot 6H_2O$), iron(II) chloride tetrahydrate ($FeCl_2 \cdot 4H_2O$), H_2SO_4 (98%), NaOH, and gallic acid (GA) were supplied by Merck KGaA, Darmstadt, Germany. Furthermore, Luria–Bertani (LB) agar was obtained from Basingstoke, Hampshire, England. Petri dishes were obtained from Sigma-Aldrich, and pathogenic strains, including *Escherichia coli* (*E. coli*) and *Staphylococcus aureus* (*S. aureus*), and the positive control ceftriaxone were sourced from the Microbiology Department, Abdul Wali Khan University, Mardan (AWKUM), Pakistan. In the experiment, waste copy paper (A4 Printing Paper, Trade International, Pakistan) was used to extract cellulose, and deionized double-distilled water (DDDW) was utilized.

2.2. Synthesis of P(MAA-*co*-AN)-*g*-MNCC

P(MAA-*co*-AN)-*g*-MNCC was prepared *via* the four steps depicted in Fig. 1. Briefly, Fe^{2+}/Fe^{3+} salts were co-precipitated under alkaline conditions in the presence of cellulose, leading to the *in situ* formation and deposition of Fe_3O_4 nanoparticles on the cellulose surface. Then, the polymerization proceeds *via* a free-radical polymerization mechanism, which is initiated by the initiator system. The vinyl group (–C=C–) of methacrylic acid participates in radical polymerization, forming the polymer backbone. The –COOH groups do not react directly with the –OH groups of cellulose under these conditions because no esterification catalyst or activation step was used. Instead, cellulose primarily serves as a substrate for grafting through radical initiation sites and physical/chemical interactions.

2.2.1. Step 1: cellulose extraction from waste printing paper. Waste printing papers (A4) were utilized for the extraction of cellulose.[42] The papers were shredded into small pieces, cleaned with DDDW, and dried in an oven at 333.15 K. The dried paper pieces (35 g) were treated with 35% v/v H_2SO_4 solution (800 mL) at 393.15 K for 20 min and then centrifuged to separate the rich cellulosic fraction. To remove the non-cellulosic fibers, the obtained material was treated with 2% w/v NaOH solution (700 mL) at 373.15 K for 1.5 h. The resultant material was bleached with 1.47 mol per kg H_2O_2 solution (1 L). At 343.15 K, the obtained product was dried in an oven for 6 h, which yielded cellulose.

2.2.2. Step 2: conversion of cellulose to nanocrystalline cellulose by acid hydrolysis. The obtained cellulose (15 g) was dispersed in DDDW (1 L) in a conical flask and stirred well on an ice bath for 30 min. To this mixture, 9.99 M H_2SO_4 solution (400 mL) was added drop-wise. The mixture was heated at 323 K

 © 2026 The Author(s). Published by the Royal Society of Chemistry

Open Access Article. Published on 23 April 2026. Downloaded on 5/22/2026 8:14:12 PM.
This article is licensed under a Creative Commons Attribution-NonCommercial 3.0 Unported Licence.

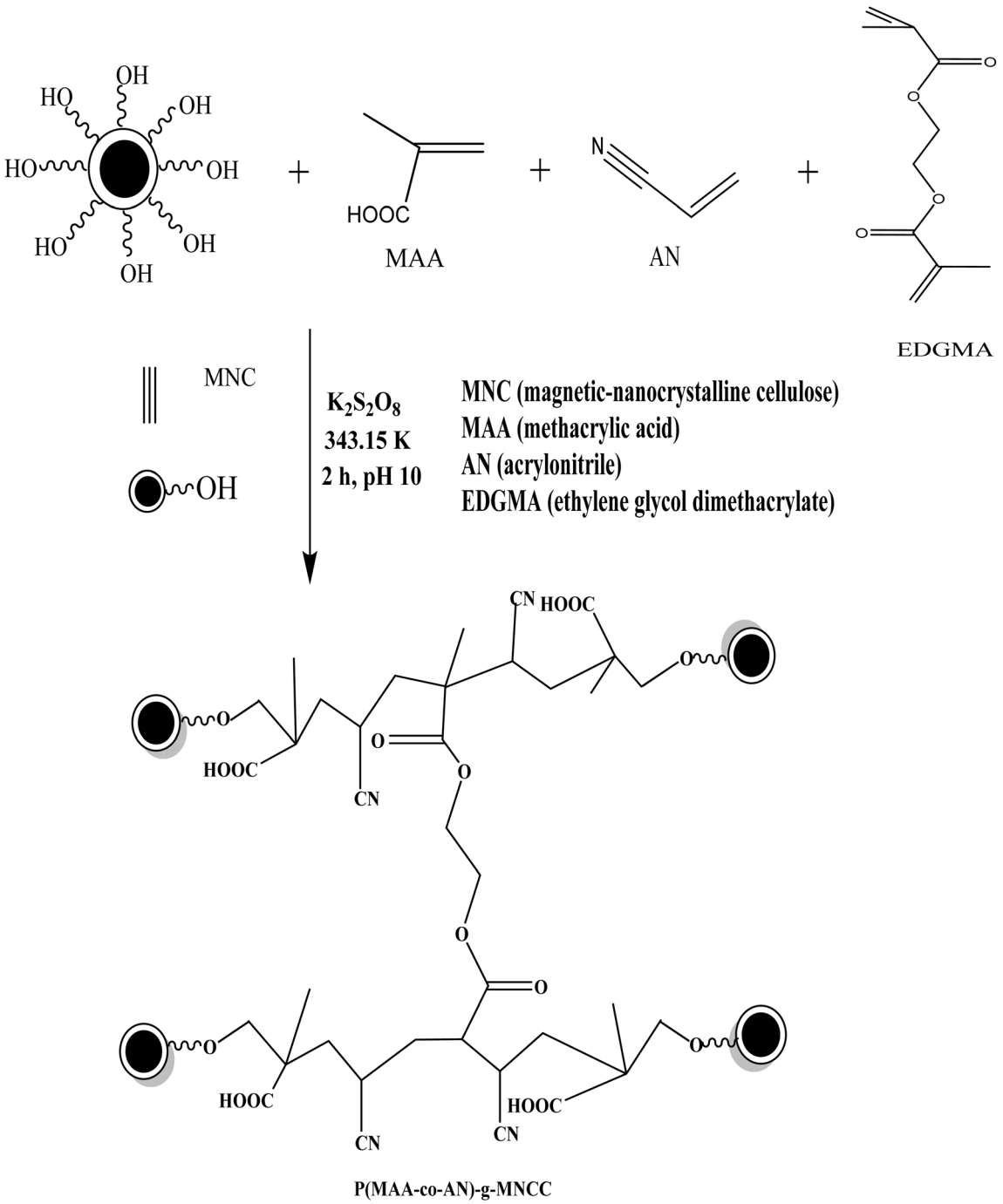

Fig. 1 General procedure for the synthesis of P(MAA-*co*-AN)-*g*-MNCC.

under vigorous stirring for 5 h and then diluted 10 times with DDDW.[24] Afterwards, the mixture was filtered, washed thoroughly with DDDW, and dried at 323 K for 4 h, which yielded nanocrystalline cellulose (NC).

2.2.3. Step 3: synthesis of magnetic nanocrystalline cellulose. Magnetic nanocrystalline cellulose (MNC) was synthesized *via* the chemical co-precipitation method.[24] Briefly, NC (2.25 g) was mixed with DDDW (300 mL) in a three-neck flask (500 mL) and purged with N_2 for 15 min. To this mixture, $FeCl_3 \cdot 6H_2O$ (2.235 g) and $FeCl_2 \cdot 4H_2O$ (1.117 g) were added, and purged again with N_2 for 20 min. After that, the mixture was heated for 20 min at 343.15 K. Co-precipitation was achieved by adding NaOH solution (2 M) dropwise until pH 10 was attained under an N_2 atmosphere with vigorous stirring using a magnetic stirrer. The orange suspension turned into a black precipitate upon completion of the reaction, and it was maintained at 333.15 K for five hours. The resultant MNC was collected by magnetic decantation, which was then thoroughly cleaned with DDDW and ethanol, and dried at 343.15 K.

Open Access Article. Published on 23 April 2026. Downloaded on 5/22/2026 8:14:12 PM. This article is licensed under a Creative Commons Attribution-NonCommercial 3.0 Unported Licence.

2.2.4. Step 4: synthesis of P(MAA-*co*-AN)-*g*-MNCC. The synthesized MNC was further modified *via* free radical graft copolymerization using AN and MAA as functional monomers. For this purpose, MNC (0.25 g) was stirred well with DDDW (50 mL) in a three-neck flask (250 mL). The mixture was purged with N_2 for 20 min and then heated at 343.15 K for 30 min. After that, $K_2S_2O_7$ (0.46 g) was added to the mixture and stirred for 10 min under an N_2 atmosphere. Next, the suspension was cooled to 313.15 K and MAA (4.25 mL), AN (3.9 mL), and EGDMA (1.4 mL) added. The pH of the system was adjusted to 10 using an NaOH solution (1 M) and heated at 343.15 K for 4 h with continuous stirring under an N_2 atmosphere. The resulting composite, P(MAA-*co*-AN)-*g*-MNCC, was filtered under suction, repeatedly cleaned with DDDW and ethanol, then dried at 333.15 K, and finally ground into powder form.

2.3. Characterization of P(MAA-*co*-AN)-*g*-MNCC

The synthesized P(MAA-*co*-AN)-*g*-MNCC was studied using various analytical techniques, including TGA, FTIR, SEM, and EDX, and its E_g, PZC, and surface area were determined (S1).

2.4. Adsorption studies

The adsorption studies were carried out in a batch setup (250 mL conical flask), where the synthesized adsorbent (0.05 g) was mixed with 100 mL GA solution (1–25 mg L^{-1}) at different pH (3–11). The mixture was shaken at 200 rpm for different intervals (2.5–35 min) at a temperature from 298.15 to 328.15 K and then centrifuged for 10 min at 9000 rpm at room temperature. After centrifugation, the aliquot was analyzed for its GA content using a UV-visible spectrophotometer (Lambda 900, PerkinElmer UV Win Lab, USA) at 259 nm. The amount of GA adsorbed (q_e) and % adsorption were determined using the following equations:[43–45]

$$q_e(\text{mg g}^{-1}) = \frac{C_o - C_e}{W} \times V \quad (1)$$

$$\text{Adsorption}(\%) = \frac{C_o - C_e}{C_o} \times 100 \quad (2)$$

where q_e (mg g^{-1}) represents the amount of GA adsorbed, C_o (mg L^{-1}) is the initial concentration of GA, C_e (mg L^{-1}) is the equilibrium concentration of GA, W (g) is the mass of the adsorbent, and V (L) denotes the volume of the GA adsorbate solution.

2.5. Kinetic, equilibrium, and thermodynamic studies

To comprehend the adsorption process, different kinetic models [pseudo-first-order, pseudo-second-order, intraparticle diffusion, and Elovich (Table S1)], equilibrium models [Freundlich, Langmuir, Temkin, and Dubinin–Radushkevich (Table S2)], and thermodynamic models [Arrhenius and van't Hoff (Table S3)] were applied.[46–48]

2.6. Desorption and reusability studies

For this purpose, the first step involved adsorbing GA on the surface of the synthesized adsorbent under optimized conditions to determine q_e and % adsorption. For the desorption study, an aqueous HCl (0.1 M) solution containing EtOH (45 vol%) was used as the desorbing agent (100 mL) at pH 2 and the mixture was shaken at 200 rpm and room temperature for 30 min. Afterwards, the mixture was centrifuged for 10 min at 9000 rpm, and the supernatant was analyzed for GA content at 259 nm using a UV-visible spectrophotometer. The amount of GA desorbed (q'_{des}) and the desorption percentage were calculated using the following equations:[49,50]

$$q'_{des}(\text{mg g}^{-1}) = \frac{C_L - C_d}{W} \times V' \quad (3)$$

$$\text{Desorption percentage} = \frac{q'_{des}}{q} \times 100 \quad (4)$$

where (q'_{des}) (mg g^{-1}) represents the quantity of GA desorbed, C_L (mg L^{-1}) denotes the GA concentration loaded on the adsorbent during adsorption, C_d (mg L^{-1}) indicates the GA concentration desorbed, W (g) is the weight of the adsorbent, and V' (L) represents the volume of the solution.

After desorption, the same adsorbent [P(MAA-*co*-AN)-*g*-MNCC] was used for four consecutive adsorption–desorption cycles.

2.7. Application to real samples

The adsorptive potential of the synthesized P(MAA-*co*-AN)-*g*-MNCC towards GA was investigated in real samples. The selected real samples include tap water, river water, industrial wastewater, and commercially available green tea. The real water samples were obtained from Mardan district, and an industrial wastewater sample from the effluent from Rashakai Special Economic Zone, Mardan, Pakistan. These samples were filtered for the removal of suspended particles and spiked with GA (10.0 mg L^{-1}). Similarly, the green tea samples (100 mg) were boiled in DDDW (100 mL) for 10 min and then filtered. These real samples were then used for the adsorptive removal of GA under the optimal conditions.

2.8. Biological applications of P(MAA-*co*-AN)-*g*-MNCC

2.8.1. Determination of antioxidant activity. The DPPH (2,2-diphenyl-1-picrylhydrazyl) assay was used to determine the antioxidant activity of the synthesized P(MAA-*co*-AN)-*g*-MNCC. Briefly, several composite concentrations (25–100 mg L^{-1}, using 5–20 mg composite) were prepared in aqueous medium. The negative control mixture was thoroughly mixed and then placed in the dark for 30 min. The absorbance of the solution was recorded at 517 nm using a double beam UV-visible spectrophotometer (A&E S90).[50] The percentage antioxidant activity was calculated using the following equation:

$$\text{Antioxidant activity percentage} = \frac{\text{Abs control} - \text{Abs sample}}{\text{Abs control}} \times 100 \quad (5)$$

© 2026 The Author(s). Published by the Royal Society of Chemistry

Open Access Article. Published on 23 April 2026. Downloaded on 5/22/2026 8:14:12 PM. This article is licensed under a Creative Commons Attribution-NonCommercial 3.0 Unported Licence.

where Abs control is the absorbance of the positive control (ascorbic acid, 10 mg L^{-1}) and Abs negative control is the absorbance of the sample.[51]

2.8.2. Antibacterial activity assessment. The antibacterial potential of the synthesized P(MAA-*co*-AN)-*g*-MNCC was evaluated against *E. coli* and *S.aureus* using the Kirby–Bauer disk diffusion method on Mueller–Hinton agar (MHA).[52] Briefly, Luria broth agar (LB agar) medium (7.41×10^3 mg L^{-1}) was sterilized by autoclaving at 121 °C (15 psi) for 15 min. Under sterile conditions, 25 mL of the medium was poured into each Petri dish and allowed to solidify. The microbial cultures were then uniformly spread across the agar surface using sterile cotton swabs to ensure confluent growth.

Three separate bores were created in each agar plate. For the treatment groups, 30 μL of the composite suspension at various concentrations (25–100 mg L^{-1}) was introduced into the bores. Ceftriaxone (10 mg L^{-1}) was utilized as a positive control in separate bores. The plates were incubated in a biochemical oxygen demand (BOD) incubator at 37 °C for 24 h. Following incubation, the antibacterial efficacy was quantified by measuring the diameter of the zones of inhibition (ZOI) in millimeters.

3. Results and discussion

3.1. Synthesis of P(MAA-*co*-AN)-*g*-MNCC

P(MAA-*co*-AN)-*g*-MNCC was synthesized through the mini-emulsion polymerization method. MNC was produced *via* chemical precipitation and subsequently integrated into NC. Graft co-polymerization of AN and MAA as functional monomers was carried out using $K_2S_2O_8$ as the radical initiator and cross-linker monomer (EDGMA) under an N_2 environment. Initially, upon heating, the persulfate initiator decomposes to produce the free radical ($KSO_4^{\bullet}$). This radical removes hydrogen from the hydroxyl group of MNC, forming an alkoxy radical. The vinyl monomer functions firstly as a radical acceptor, resulting in chain growth. After that, it functions as a radical donor for other monomers. In chain propagation, the end vinyl groups of EGDMA react with the polymeric chain, forming a three-dimensional network structure with –COOH and –C≡N functionalities. Compared to AN, MAA, a vinyl monomer with higher hydrophilicity, interacts more rapidly with MNC due to its hydrophilic hydroxyl group.

The yield of the P(MAA-*co*-AN)-*g*-MNCC synthesis was determined to be 84.6%. This was calculated by comparing the weight of the final dried and purified composite against the total mass of the initial MNC and monomers used in the feed.

The degree of swelling was evaluated gravimetrically in distilled water. The composite exhibited an equilibrium swelling capacity of 12.4 g g^{-1}. The presence of hydrophobic acrylonitrile units and the EGDMA crosslinking network endows this material with structural integrity while maintaining sufficient porosity for adsorption.

The degree of crosslinking was determined based on the molar ratio of the EGDMA crosslinker to the total monomer concentration in the feed. The crosslinking density was calculated to be 0.078 mol%. This level of crosslinking ensures a robust three-dimensional network that prevents the dissolution of the copolymer during application in aqueous media.

3.2. Characterization of P(MAA-*co*-AN)-*g*-MNCC

Fig. 2a shows the FTIR spectrum of P(MAA-*co*-AN)-*g*-MNCC, displaying characteristic peaks at 538 cm^{-1}, 592 cm^{-1}, 589 cm^{-1}, and 632 cm^{-1} attributed to the vibration of iron oxide in Fe_3O_4 nanoparticles. The peak at 2922 cm^{-1} is associated with the stretching vibration of the –CH group. Additionally, the peaks at 1114 cm^{-1} and 1636 cm^{-1} indicate the presence of a saccharide structure and glycosidic linkage in cellulose.[53–55] The peak at 1551 cm^{-1} is attributed to the stretching vibration of the C=C group.[54,56] In the spectrum, a broad O–H stretching band appears at 3441–3256 cm^{-1}.[24] The peaks at 1217 cm^{-1} and 1700 cm^{-1} indicate the presence of –C–O and –C=O groups, confirming the existence of hydroxyl and carboxylic acid groups in the synthesized composite, respectively.[57] Additionally, some new peaks appear compared to the spectra of the monomers and the Fe_3O_4/cellulose precursor.

SEM was used to analyze the morphology and structure of P(MAA-*co*-AN)-*g*-MNCC, as depicted in Fig. 2c. The SEM image of P(MAA-*co*-AN)-*g*-MNCC appears undulant and coarse. The increase in the amount of Fe_3O_4 inside the cellulose network resulted in an evident increase in surface roughness, which greatly contributed to the increased surface area. SEM analysis was explicitly performed for studying the surface topology, porosity, and morphology of P(MAA-*co*-AN)-*g*-MNCC.

The elemental composition of P(MAA-*co*-AN)-*g*-MNCC was analyzed using EDX analysis (Fig. 2d). The EDX spectrum of the synthesized composite shows the presence of C, Fe, O, and N, indicating the efficient synthesis of P(MAA-*co*-AN)-*g*-MNCC. EDX confirms the elemental incorporation and homogeneous distribution, while successful network formation is supported collectively by the FTIR analysis, swelling behavior, and adsorption performance rather than elemental composition alone.

The thermal stability of P(MAA-*co*-AN)-*g*-MNCC was analyzed by TGA, as can be seen in Fig. 2e. It is evident from the curve that the decomposition of P(MAA-*co*-AN)-*g*-MNCC occurs at various stages. The first weight loss (below ~120 °C) corresponds to moisture removal. The second stage (≈220–350 °C) is attributed mainly to the degradation of its cellulose backbone.

The subsequent weight loss at higher temperatures corresponds to the degradation of the grafted P(MAA-*co*-AN) network.[58,59]

The band gap energy for P(MAA-*co*-AN)-*g*-MNCC was determined by the Tauc method (Fig. 2f), which was found to be 2.30 eV. This band gap energy value provides support for the adsorptive nature of P(MAA-*co*-AN)-*g*-MNCC.

The PZC was determined to investigate the influence of pH on the surface properties of P(MAA-*co*-AN)-*g*-MNCC and its adsorption behavior. By plotting ΔpH *vs.* pH_i, the PZC of the synthesized material was calculated to be about 8.9 (Fig. 2g). This result showed that the synthesized material carries a positive charge at pH below 8.9 and a negative charge at pH above 8.9, and *vice versa*. GA has four pK_a values: 4.16, 8.55, 11.40, and 12.8, indicating that it has a negative charge at pH

Open Access Article. Published on 23 April 2026. Downloaded on 5/22/2026 8:14:12 PM.
This article is licensed under a Creative Commons Attribution-NonCommercial 3.0 Unported Licence.

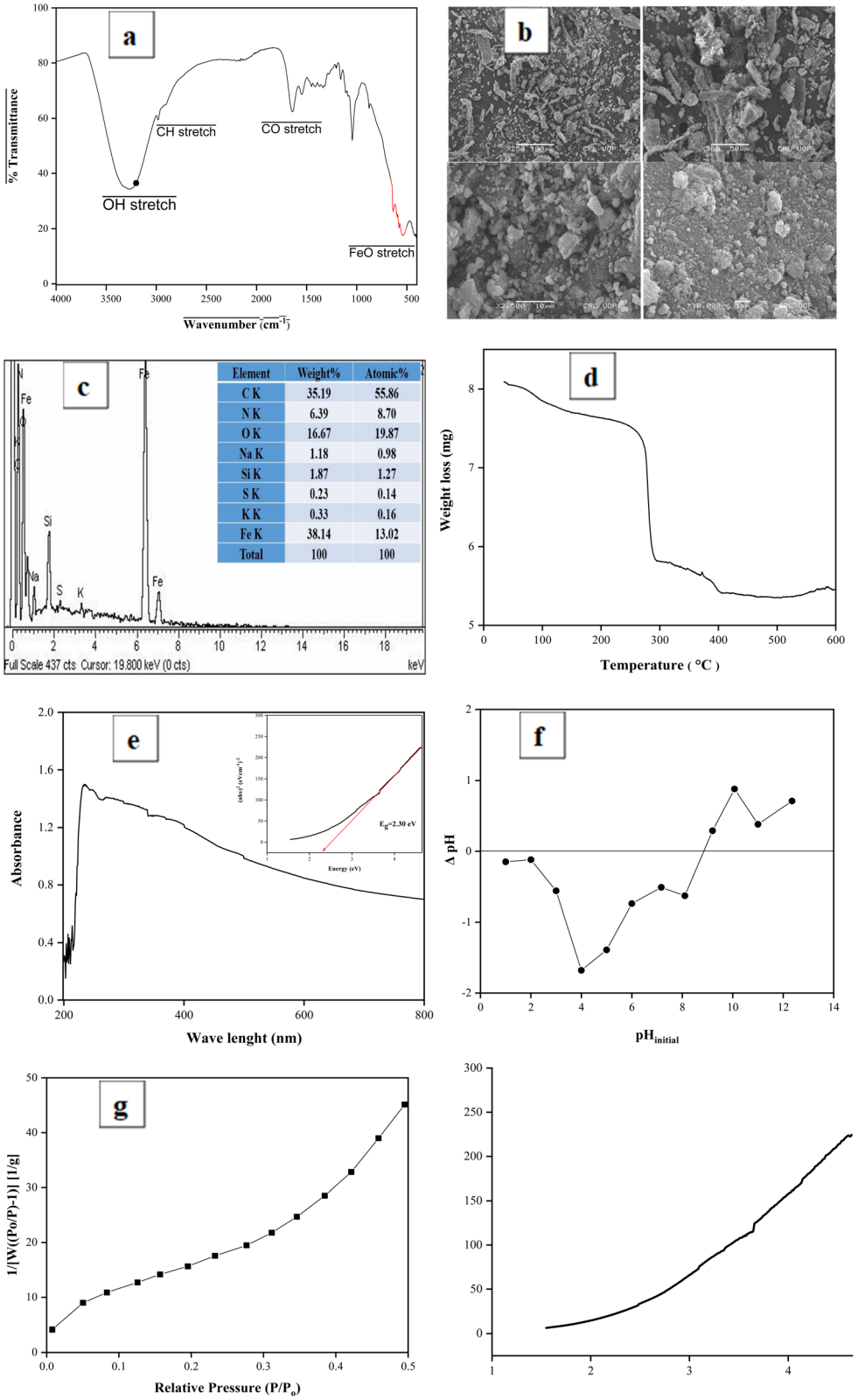

Fig. 2 Characterization of P(MAA-*co*-AN)-*g*-MNCC: (a) FTIR spectrum, (b) SEM images, (c) EDX spectrum, (d) TGA pattern, (e) UV-visible spectrum and band gap energy determination, (f) determination of PZC and (g) surface area analysis.

greater than 4.16.[37] The results confirmed the presence of an electrostatic contact force between GA and P(MAA-*co*-AN)-*g*-MNCC at pH 7.

The surface properties of P(MAA-*co*-AN)-*g*-MNCC were analyzed by recording its N_2 gas adsorption–desorption isotherms at 77.35 K using a surface area analyzer. The Brunauer–Emmett–Teller

© 2026 The Author(s). Published by the Royal Society of Chemistry

Open Access Article. Published on 23 April 2026. Downloaded on 5/22/2026 8:14:12 PM. This article is licensed under a Creative Commons Attribution-NonCommercial 3.0 Unported Licence.

(BET) equation was employed to calculate the surface area of the composite. The de Boer method was used to calculate the pore radius and volume of the composite. According to the results, the synthesized composite possesses a surface area of about 46.034 $m^2 g^{-1}$, a pore radius of 16.231 Å, and a pore volume of 0.001 $cm^3 g^{-1}$. The surface area of the synthesized composite was reduced because of the presence of multiple functional groups. Fig. 2h illustrates the adsorption–desorption isotherm of the synthesized material, which is a type IV isotherm.

3.3. Adsorption of GA using P(MAA-*co*-AN)-*g*-MNCC

3.3.1. Effect of time. The adsorption of GA onto P(MAA-*co*-AN)-*g*-MNCC was studied at different contact times with a concentration of 10 mg L^{-1} (Fig. 3a). The results indicated that the adsorption increased with time, and after 30 min, it did not increase further. Initially, the adsorption capacity was fast, which may be attributed to the existence of a large number of active sites for adsorption, and decreased with time because of saturation of the binding sites. Equilibrium was reached after 30 min, and thus it was considered the optimum time for adsorption experiments.

3.3.2. Effect of pH. The effect of pH on the adsorption process was evaluated by adjusting the pH of the medium from pH 3 to pH 11 while keeping the GA concentration constant at 10.27 mg L^{-1}. The results are shown in Fig. 3b, indicating that pH has a significant influence on the adsorption of GA on P(MAA-*co*-AN)-*g*-MNCC, with the highest adsorption being observed at pH of 7.0. At pH 7.0, GA exists as a negatively charged molecule, while the surface of the synthesized material [P(MAA-*co*-AN)-*g*-MNCC] carries a positive charge, which enhances the electrostatic interactions and promotes the adsorption phenomena. Particularly, at low pH levels, reduced adsorption is likely due to the electrostatic repulsion between the positively charged GA and P(MAA-*co*-AN)-*g*-MNCC. As the pH increases, both GA and the adsorbent become more ionized. Thus, the surface of P(MAA-*co*-AN)-*g*-MNCC becomes positively charged at a pH level below 8.9. A slight increase in GA adsorption within the pH range of 3.0 to 7 was observed. Adsorption significantly increased from pH 3 to 7 due to the reduced electrostatic repulsion and increased availability of active sites as the ionization state of gallic acid changes. At pH 7.0, the amount of GA adsorbed was found to be 15.65 mg g^{-1} with a percentage adsorption (% adsorption) of 76.35% for the initial concentration of GA of 10.27 mg L^{-1}. This finding indicates that the adsorption of GA on P(MAA-*co*-AN)-*g*-MNCC occurs *via* an exchange mechanism.[60] The GA molecule was absorbed on the surface of P(MAA-*co*-AN)-*g*-MNCC by releasing a proton.[24] Considering the electrostatic interaction between the positively charged P(MAA-*co*-AA)-*g*-MNCC (adsorbent) and the negatively charged GA (adsorbate), the pH was kept at 7.0 for subsequent experiments.

3.3.3. Effect of temperature. Fig. 3c illustrates the effect of temperature on the adsorption of GA onto the P(MAA-*co*-AN)-*g*-MNCC surface within the range of 25 °C to 55 °C (298 K to 328 K). Variations in temperature had a negligible influence within this studied range. The adsorptive removal percentage of GA

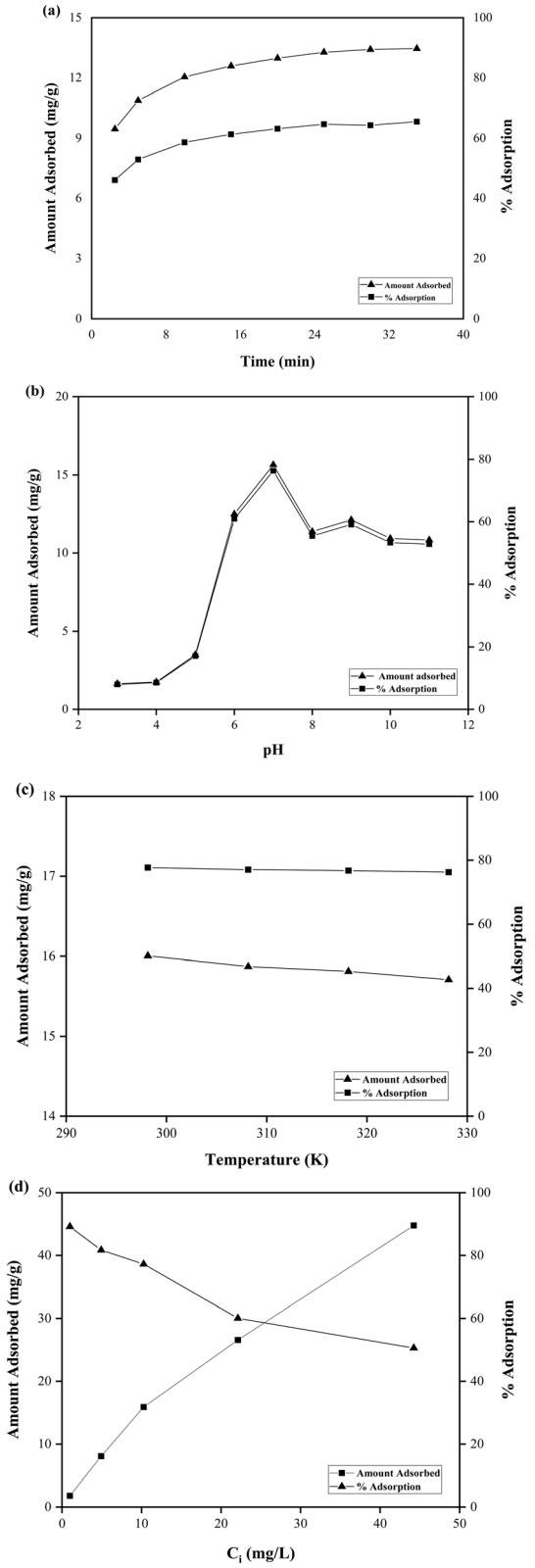

Fig. 3 Effect of adsorption parameters: (a) time, (b) pH, (c) temperature and (d) GA concentration.

decreased slightly as the temperature increased, indicating the exothermic nature of the adsorption process. At 25 °C (298.15 K), the adsorption capacity was 16.01 mg g^{-1} (77.68% removal)

Open Access Article. Published on 23 April 2026. Downloaded on 5/22/2026 8:14:12 PM.
This article is licensed under a Creative Commons Attribution-NonCommercial 3.0 Unported Licence.

for an initial GA concentration of 10.27 mg L^{-1}. Consequently, 25 °C was selected as the optimal temperature for further experiments.

3.3.4. Effect of adsorbate concentration. The effect of the initial concentration of GA on P(MAA-*co*-AN)-*g*-MNCC was investigated by varying the initial concentration of the adsorbate at pH 7.0. The results, as depicted in Fig. 3d, indicate that the adsorption capacity is influenced by the initial concentration of the adsorbate, playing a significant role in the adsorption process. Initially, adsorption occurred rapidly as GA molecules attached to the external surface. Subsequently, as the molecules penetrated the pores (internal surface), the process slowed down. The quick initial adsorption capacity may result from the abundant binding sites available for adsorption. Conversely, the slower rates observed toward the end can be attributed to the saturation of these binding sites and the attainment of equilibrium.[60,61] This study revealed that with an increase in GA concentration from 1–45 mg L^{-1}, the adsorption percentage decreased from 89.19% to 50.60%, while the adsorbed amount increased from 1.80 mg g^{-1} to 44.77 mg g^{-1}. This indicates that the adsorbent has a finite number of active sites that reach saturation at a particular concentration.[60,61]

3.4. Kinetic, equilibrium, and thermodynamic studies

The results indicate that the data were well-suited to the pseudo-second-order kinetic model, as evidenced by the high

Table 1 Kinetics, equilibrium and thermodynamic model parameters for the adsorption of GA in an aqueous environment using P(MAA-*co*-AN)-*g*-MNCC[a]

Model	Parameter	Unit	Value
Kinetic models			
Pseudo-first-order kinetic	q_e (calculated)	mg g^{-1}	15.890
	K_1	min^{-1}	0.285
	R^2	—	0.869
Pseudo-first-order kinetic	q_e (calculated)	mg g^{-1}	14.010
	K_2	g mg^{-1} min^{-1}	0.049
	H	mg g^{-1} min^{-1}	9.170
	R^2	—	0.999
Intraparticle diffusion	K_{int}	mg g^{-1} $min^{-1/2}$	0.879
	C	—	8.776
	R^2	—	0.894
Elovich	A	mg g^{-1} min^{-1}	2.161
	B	g mg^{-1}	0.655
	R^2	—	0.981
Equilibrium			
Freundlich	K_F (calculated)	mg g^{-1}	7.761
	n	L g^{-1}	1.668
	$1/n$	g L^{-1}	0.600
	R^2	—	0.982
Langmuir	Q_o (calculated)	mg g^{-1}	52.460
	K_L	L g^{-1}	10.171
	a_L	L g^{-1}	0.194
	R_L	g L^{-1}	0.0023–0.089
	R^2	—	0.9300
Temkin	B_T (calculated)	mg g^{-1}	7.691
	A_T	L g^{-1}	5.849
	b_T	J mol^{-1}	322.15
	R^2	—	0.840
Dubinin–Radushkevich (D–R)	Q_m (calculated)	mg g^{-1}	21.913
	K	mol^2 kJ^{-2}	7.81×10^{-8}
	E	kJ mol^{-1}	12.903
	R^2	—	0.750

Thermodynamic

Temperature (K)	$\Delta G°$ (kJ mol^{-1})	$\Delta H°$ (kJ mol^{-1})	$\Delta S°$ (kJ mol^{-1})
298.15	−4.810	−2.113	0.009
308.15	−4.877		
318.15	−4.992		
328.15	−5.072		

[a] The experimental q_e value is 15.886 mg g^{-1}.

© 2026 The Author(s). Published by the Royal Society of Chemistry

Open Access Article. Published on 23 April 2026. Downloaded on 5/22/2026 8:14:12 PM. This article is licensed under a Creative Commons Attribution-NonCommercial 3.0 Unported Licence.

linear regression coefficient (R^2) value shown in Table 1. The details of the various equations used for the determination of the kinetic and thermodynamic parameters are given in the SI (Tables S1–S3), while the data obtained are shown in Fig. S1–S11 in the SI. Fig. 4 and 5 present the pseudo-second-order kinetics and the Freundlich adsorption isotherm studies, respectively. The results indicated that the adsorption rate increased in direct proportion to the square of the number of vacant sites, suggesting that ionic interactions or ion-exchange mechanisms control the adsorption process. The pseudo-second-order adsorption mechanism primarily comprises two steps. The first step is external diffusion, where GA molecules move from the solution bulk to the external surface of P(MAA-*co*-AN)-*g*-MNCC. This is followed by the adsorption of the adsorbate molecules on the adsorbent surface, likely due to ionic interactions.

The data fit the Freundlich adsorption model well, as indicated by the high linear regression coefficient (R^2) value in Table 1. This suggests a heterogeneous surface with a non-uniform distribution of the heat of adsorption, making this model appropriate for such a highly heterogeneous surface. The Freundlich equation implies that as the adsorption sites on an adsorbent become saturated, the adsorption energy decreases exponentially. K_L and a_L are associated with the maximum adsorption capacity (L g^{-1}) and bonding strength (L g^{-1}), respectively. The R_L value determines whether the isotherm is unfavorable ($R_L > 1$), linear ($R_L = 1$), favorable ($0 < R_L < 1$), or irreversible ($R_L = 0$). R_L values ranging from 0 to 1 indicate favorable adsorption. In this study, the R_L values are greater than zero and less than one, confirming the favorable nature of GA adsorption on P(MAA-*co*-AN)-*g*-MNCC. The constant K, which is related to the adsorption energy, was calculated to be 0.003 mol^2 kJ^{-2}, resulting in a computed E value of 12.903 kJ mol^{-1}, using P(MAA-*co*-AN)-*g*-MNCC. It has been reported that when the mean adsorption energy (E) is less than

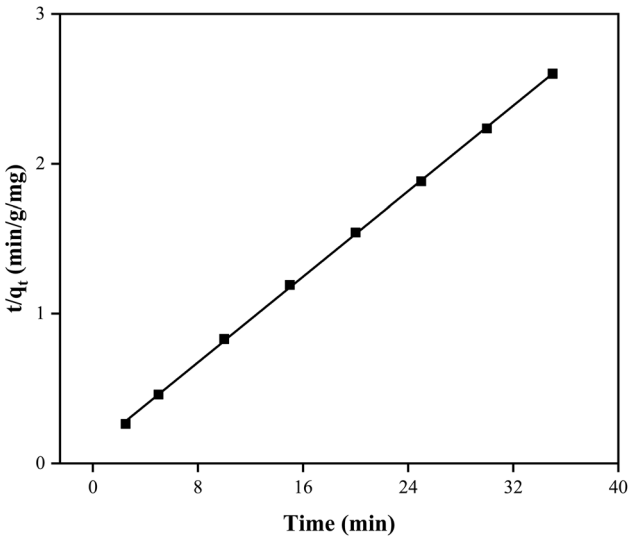

Fig. 4 Pseudo-second-order kinetic model for the adsorption of GA using P(MAA-*co*-AN)-*g*-MNCC.

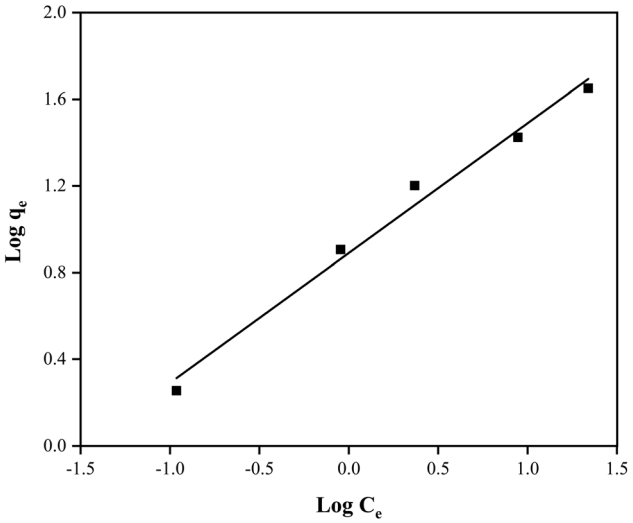

Fig. 5 Freundlich isotherm for the adsorption of GA using P(MAA-*co*-AN)-*g*-MNCC.

8 kJ mol^{-1}, it indicates physical adsorption. In comparison, values between 8 and 16 kJ mol^{-1} suggest chemical ion-exchange, and values above 40 kJ mol^{-1} indicate chemical adsorption. In this study, the lower E values indicate that the removal of GA from the aqueous environment mainly occurs through chemical adsorption and ion-exchange processes.

Based on the data obtained, the values of $\Delta G°$, $\Delta H°$, and $\Delta S°$ were calculated and listed in Table 1. The negative $\Delta G°$ value indicates that the adsorption process is spontaneous and exothermic, involving an ion-exchange mechanism. Furthermore, the decrease in $\Delta G°$ as the temperature increases suggests a higher adsorption capacity at lower temperatures. An increase in temperature causes GA molecules to move more rapidly, causing them to move from the solid medium to the liquid medium. As a result, the adsorption of GA decreases. This trend is also reflected in the K_D values. The negative $\Delta H°$ values indicate that the adsorption process is exothermic, suggesting that adsorption may be more favorable at lower temperatures and confirming the occurrence of physisorption. The positive value of $\Delta S°$ (0.009 kJ K^{-1} mol^{-1}) indicates an increase in randomness at the solid–liquid interface during the sorption of GA on P(MAA-*co*-AN)-*g*-MNCC. Additionally, the activation energy (E_a) and sticking probability (S^*) parameters are used to determine whether the adsorption process is primarily chemical or physical in nature. The findings are shown in Fig. 4, with

Table 2 Reusability and real sample applications of P(MAA-*co*-AN)-*g*-MNCC for the adsorption of GA

Reusability		Real sample applications	
Batch	% adsorption	Real sample	% adsorption
1st	77.1 ± 2.51	Tap water	78.3 ± 2.56
2nd	76.3 ± 2.43	River water	75.2 ± 2.14
3rd	75.1 ± 2.51	Industrial wastewater	70.3 ± 1.99
4th	73.5 ± 2.16	Green tea	84.9 ± 3.01

© 2026 The Author(s). Published by the Royal Society of Chemistry

Open Access Article. Published on 23 April 2026. Downloaded on 5/22/2026 8:14:12 PM. This article is licensed under a Creative Commons Attribution-NonCommercial 3.0 Unported Licence.

Table 3 Antioxidant and antibacterial activities of P(MAA-*co*-AN)-*g*-MNCC at various concentrations

P(MAA-*co*-AN)-*g*-MNCC concentration (mg L^{-1})	Antioxidant activity (% DPPH scavenging)	Antibacterial activity (zone of inhibition in mm)	
		Escherichia coli	*Staphylococcus aureus*
25	58 ± 1.2	3.9 ± 0.12	4.2 ± 0.11
50	61 ± 1.5	4.3 ± 0.20	5.1 ± 0.13
75	68 ± 1.8	6.2 ± 0.18	6.4 ± 0.22
100	77 ± 2.2	7.1 ± 0.22	7.5 ± 0.19

the E_a and S^* values determined from the slope and intercept, respectively. The calculated E_a value is 1.263 kJ mol^{-1}, indicating that physicochemical and ion exchange mechanisms might be dominant. Similarly, in the case of a favorable system, the S^* value should be greater than zero but less than one ($0 < S^* < 1$). The S^* value in this study was determined to be 0.144, indicating that the adsorbate (GA) adhered favorably to the synthesized adsorbent [P(MAA-*co*-AN)-*g*-MNCC] (Table 1).

3.5. Desorption and reusability studies

A desorption batch experiment was designed to study the reusable potential of the synthesized P(MAA-*co*-AN)-*g*-MNCC. It was found that during the desorption process, >98% of the adsorbed GA was desorbed, and the same adsorbent was reused in four consecutive adsorption–desorption cycles, maintaining excellent adsorption capacity (Table 2). From the first to the fourth batch of adsorption–desorption process, the overall decrease in the % adsorption was <4%. This confirms the effective recyclable and reusable nature of the synthesized P(MAA-*co*-AN)-*g*-MNCC.

3.6. Application to real samples

The removal of GA from real samples was investigated. For this purpose, two real samples (river water and tap water), one from industrial effluent from the Rashakai Special Economic Zone, and one Lipton green tea sample, were utilized. The amount of GA adsorbed, q_e, and the adsorption percentage were determined, as shown in Table 2. The result shows the efficient removal of GA from the real samples. This confirms the applicability of P(MAA-*co*-AN)-*g*-MNCC for the treatment of real samples and industrial waste.

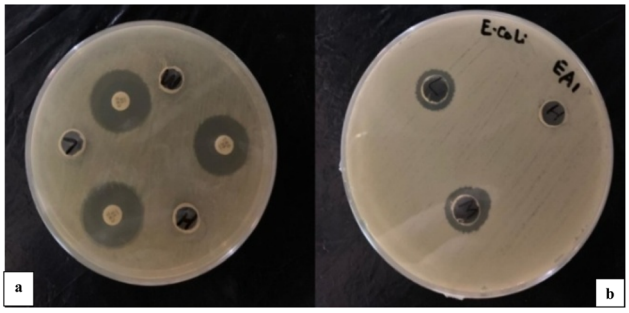

Fig. 6 Antibacterial activity of P(MAA-*co*-AN)-*g*-MNCC against (a) *Escherichia coli* and (b) *Staphylococcus aureus*.

3.7. Biological applications of P(MAA-*co*-AN)-*g*-MNCC

3.7.1. Antioxidant activity. The free radical scavenging (antioxidant) activity of P(MAA-*co*-AN)-*g*-MNCC was investigated at various concentrations (25–100 mg L^{-1}). DPPH, an organic compound, was used to evaluate its free radical scavenging activity. Table 3 presents the antioxidant activity of the synthesized composite. The results show that the % inhibition accelerated with an increase in the concentration of the composite. The synthesized composite exhibited significant antioxidant activity, scavenging DPPH radicals by 58 ± 1.2%, 61 ± 1.5%, 68 ± 1.8%, and 77 ± 2.2% at various tested concentrations, respectively.

3.7.2. Antibacterial activity. The antibacterial efficacy of P(MAA-*co*-AN)-*g*-MNCC with DDDW was evaluated using the agar well diffusion technique. The composite exhibited strong antibacterial properties against two harmful bacteria: *E. coli* (a Gram-negative bacterium) and *S. aureus* (a Gram-positive bacterium). The synthesized composite formed a zone of inhibition against *S. aureus* and *E. coli*. The positive control ceftriaxone exhibited excellent activity against *E. coli* with an inhibition zone of 12 mm, while the synthesized composite was found to be effective against both *E. coli* and *S. aureus*, as shown in Table 3. It was found that with an increase in the concentration of the composite (25–100 mg L^{-1}), the zone of inhibition also increased, *i.e.*, 3.9 ± 0.12 to 7.1 ± 0.22 against *E. coli* and 4.2 ± 0.11 to 7.5 ± 0.19 against *S. aureus*. The antibacterial activity was found to be higher against *S. aureus* (Gram-positive) compared to *E. coli* (Gram-negative) (Fig. 6). This demonstrates the effective antibacterial nature of the as-synthesized P(MAA-*co*-AN)-*g*-MNCC.

4. Conclusions

In this study, a novel P(MAA-*co*-AN)-*g*-MNCC composite was successfully engineered using a robust stepwise and free-radical graft co-polymerization strategy. Comprehensive characterization confirmed the structural integrity and high density of active functional groups within the composite, which directly contributed to its superior performance. This material demonstrated exceptional multi-functionality, exhibiting high efficiency in the removal of gallic acid (GA) from complex water and wastewater matrices, alongside potent antioxidant and

 © 2026 The Author(s). Published by the Royal Society of Chemistry

Open Access Article. Published on 23 April 2026. Downloaded on 5/22/2026 8:14:12 PM. This article is licensed under a Creative Commons Attribution-NonCommercial 3.0 Unported Licence.

antibacterial activities. Notably, the high recyclability and biological stability of P(MAA-*co*-AN)-*g*-MNCC suggest that it is a sustainable alternative to conventional sorbents. These findings highlight the potential of this composite not only for advanced wastewater treatment but also as a versatile platform for controlled drug release, solid-phase extraction, and biomedical applications.

Author contributions

Ali Khan: methodology, formal analysis, writing – original draft, Hamayun Khan: conceptualization, supervision, project administration, writing – review & editing. Nasrullah Shah: conceptualization, supervision, project administration, writing – review & editing. Mahmoud Elodemi: formal analysis, software, validation, data curation. S. Tasqeeruddin: validation, software, formal analysis and writing – review & editing, funding acquisition, resources, Ajmal Khan: writing – review & editing, supervision & project administration, Ahmed Al-Harrasi: writing – review & editing, supervision & project administration.

Conflicts of interest

The authors declare no conflict of interest.

Data availability

The data supporting this article have been included as part of the supplementary information (SI). Supplementary information: (a) procedure and details of instruments used in characterization techniques. (b) data (tables and plots) obtained by applying kinetic, equilibrium and thermodynamic models. See DOI: https://doi.org/10.1039/d6ra00474a.

Acknowledgements

The authors extend their appreciation to the Deanship of Research and Graduate Studies at King Khalid University, KSA, for funding this work through Small Research Group Project under grant number (RGP.1/73/46).

References

1 A. Dias, A. Hussain, A. S. Marcos and A. C. A. Roque, A biotechnological perspective on the application of iron oxide magnetic colloids modified with polysaccharides, *Biotechnol. Adv.*, 2011, **29**, 142–155.
2 P. R. Chang, J. Yu, X. Ma and D. P. Anderson, Polysaccharides as stabilizers for the synthesis of magnetic nanoparticles, *Carbohydr. Polym.*, 2011, **83**, 640–644.
3 H. Hu, H. Liu, D. Zhang, J. Wang and X. Zhang, pH and electromagnetic dual-remoted drug delivery based on bimodal super paramagnetic Fe_3O_4@porous silica nanoparticles, *Eng. Sci.*, 2018, **2**, 43–48.
4 M. A. C. M. Haniffa, Y. C. Ching, H. A. Illias, K. Munawar, S. Ibrahim, D. H. Nguyen and C. H. Chuah, Cellulose supported promising magnetic sorbents for magnetic solid-phase extraction: A review, *Carbohydr. Polym.*, 2021, **253**, 117245.
5 H. Khan, A. K. Khalil, A. Khan, K. Saeed and N. Ali, Photocatalytic degradation of bromophenol blue in aqueous medium using chitosan conjugated magnetic nanoparticles, *Korean J. Chem. Eng.*, 2016, **33**, 2802–2807.
6 A. Aseri, S. K. Garg, A. Nayak and J. Ahsan, Magnetic nanoparticles: magnetic nano-technology using biomedical applications and future prospects, *Int. J. Pharm. Sci. Rev. Res.*, 2015, **31**, 119–131.
7 B. G. Maciel, R. J. da Silva, A. E. Chávez-Guajardo, J. C. Medina-Llamas, J. J. Alcaraz-Espinoza and C. P. de Melo, Magnetic extraction and purification of DNA from whole human blood using a γ-Fe_2O_3@chitosan@polyaniline hybrid nanocomposite, *Carbohydr. Polym.*, 2018, **197**, 100–108.
8 I. A. Perales, L. M. P. Pineda, L. M. Lozano-Sánchez, J. G. Puente-Cordova and A. Elías-Zúñiga, Enhancement of a magnetorheological PDMS elastomer with carbonyl iron particles, *Polym. Test.*, 2017, **57**, 78–86.
9 S. J. Kiprono, M. W. Ullah and G. Yang, Encapsulation of E. coli in biomimetic and Fe_3O_4-doped hydrogel: structural and viability analyses, *Appl. Microbiol. Biotechnol.*, 2018, **102**, 933–944.
10 M. W. Ullah, Z. Shi, X. Shi, D. Zeng, S. Li and G. Yang, Microbes as structural templates in biofabrication: Study of surface chemistry and applications, *ACS Sustain. Chem. Eng.*, 2017, **5**, 11163–11175.
11 A. S. Thakor and S. S. Gambhir, Nanooncology: the future of cancer diagnosis and therapy, *Ca-Cancer J. Clin.*, 2013, **63**(6), 395–418.
12 C. W. Leung, K. Y. Chan, W. K. Chan, W. Zhong and P. W. T. Pong, Effect of synthesis conditions on the properties of citric-acid coated iron oxide nanoparticles, *Microelectron. Eng.*, 2013, **110**, 329–334.
13 G. Kandasamy, A. Sudame, P. Bhati, A. Chakrabarty, S. Kale and D. Maity, Systematic magnetic fluid hyperthermia studies of carboxyl functionalized hydrophilic superparamagnetic iron oxide nanoparticles based ferrofluids, *J. Colloid Interface Sci.*, 2018, **514**, 534–543.
14 Z. Shaterabadi, G. Nabiyouni and M. Soleymani, High impact of in-situ dextran coating on biocompatibility, stability and magnetic properties of iron oxide nanoparticles, *Mater. Sci. Eng.*, 2017, **75**, 947–956.
15 E. Rauwel, S. Al-Arag, H. Salehi, C. O. Amorim, F. Cuisinier, M. Guha and P. Rauwel, Assessing cobalt metal nanoparticles uptake by cancer cells using live Raman spectroscopy, *Int. J. Nanomed.*, 2020, **15**, 7051.
16 H. Khan, A. K. Khalil and A. Khan, Photocatalytic degradation of alizarin yellow in aqueous medium and real samples using chitosan conjugated tin magnetic nanocomposites, *J. Mater. Sci.: Mater. Electron.*, 2019, **30**, 21332–21342.
17 G. Salmanian, S. A. Hassanzadeh-Tabrizi and N. Koupaei, Magnetic chitosan nanocomposites for simultaneous

Open Access Article. Published on 23 April 2026. Downloaded on 5/22/2026 8:14:12 PM. This article is licensed under a Creative Commons Attribution-NonCommercial 3.0 Unported Licence.

hyperthermia and drug delivery applications: A review, *Int. J. Biol. Macromol.*, 2021, **184**, 618–635.

18 X. Sun, S. Wang, Y. Wang and K. Sun, Synthesis and characterization of hydrophobic Fe_3O_4 magnetic nanoparticles with high saturation magnetization, *J. Supercond. Novel Magn.*, 2019, **32**, 2903–2911.

19 S. Khan, Z. Shah, S. Riaz, N. Ahmad, S. Islam, M. A. Raza and S. Naseem, Antimicrobial activity of citric acid functionalized iron oxide nanoparticles-superparamagnetic effect, *Ceram. Int.*, 2020, **46**, 10942–10951.

20 S. M. Fotukian, A. Barati, M. Soleymani and A. M. Alizadeh, Solvothermal synthesis of $CuFe_2O_4$ and Fe_3O_4 nanoparticles with high heating efficiency for magnetic hyperthermia application, *J. Alloys Compd.*, 2020, **816**, 152548.

21 A. Barra, Z. Alves, N. M. Ferreira, M. A. Martins, H. Oliveira, L. P. Ferreira and P. Ferreira, Biocompatible chitosan-based composites with properties suitable for hyperthermia therapy, *J. Mater. Chem.*, 2020, **8**, 1256–1265.

22 M. A. Dheyab, A. A. Aziz, M. S. Jameel, O. A. Noqta and B. Mehrdel, Synthesis and coating methods of biocompatible iron oxide/gold nanoparticle and nanocomposite for biomedical applications, *Chin. J. Phys.*, 2020, **64**, 305–325.

23 X. Huang, J. Zhuang, D. Chen, H. Liu, F. Tang, X. Yan and J. Ren, General strategy for designing functionalized magnetic microspheres for different bioapplications, *Langmuir*, 2009, **25**, 11657–11663.

24 T. S. Anirudhan and S. R. R. J. Binusree, Adsorptive separation of myoglobin from aqueous solutions using iron oxide magnetic nanoparticles modified with functionalized nanocrystalline cellulose, *J. Chem. Eng. Data*, 2013, **58**, 1329–1339.

25 J. Hu, G. Chen and I. M. Lo, Removal and recovery of Cr (VI) from wastewater by maghemite nanoparticles, *Water Res.*, 2005, **39**(18), 4528–4536.

26 M. M. Woldeamanuel, S. Mohapatra, S. Senapati, T. K. Bastia, A. K. Panda and P. Rath, Role of magnetic nanomaterials in environmental remediation, in *Iron Oxide-Based Nanocomposites and Nanoenzymes: Fundamentals and Applications*, Springer International Publishing, Cham, 2024, pp. 185–208.

27 D. Klemm, B. Heublein, H. P. Fink and A. Bohn, Cellulose: fascinating biopolymer and sustainable raw material, *Angew. Chem., Int. Ed.*, 2005, **44**(22), 3358–3393.

28 Y. Habibi, L. A. Lucia and O. J. Rojas, Cellulose nanocrystals: chemistry, self-assembly, and applications, *Chem. Rev.*, 2010, **110**(6), 3479–3500.

29 L. Ding, C. Guo, Y. Zhu, L. Ma, Y. Kong, M. Zhong and H. Zhang, Adsorptive removal of gallic acid from aqueous solution onto magnetic ion exchange resin, *Water Sci. Technol.*, 2020, **81**, 1479–1493.

30 K. Kerdsomboon, W. Chumsawat and C. Auesukaree, Effects of *Moringa oleifera* leaf extracts and its bioactive compound gallic acid on reducing toxicities of heavy metals and metalloid in *Saccharomyces cerevisiae*, *Chemosphere*, 2021, **270**, 128659.

31 S. Verma, A. Singh and A. Mishra, Gallic acid molecular rival of cancer, *Environ. Toxicol. Pharmacol.*, 2013, **35**, 473–485.

32 Y. Hao, R. Gao, D. Liu, Y. Tang and Z. Guo, Selective extraction of gallic acid in pomegranate rind using surface imprinting polymers over magnetic carbon nanotubes, *Anal. Bioanal. Chem.*, 2015, **407**, 7681–7690.

33 X. Tang, G. I. Urujeni, X. Ni, Z. Lu, D. Wang, J. Gao and P. Dramou, Polyethyleneimine in designed nanocomposite based magnetic halloysite nanotubes for extraction and determination of gallic acid in green tea, *Int. J. Biol. Macromol.*, 2024, **265**, 130914.

34 F. Ferk, A. Chakraborty, W. Jäger, M. Kundi, J. Bichler, M. Mišík and C. Hoelzl, Potent protection of gallic acid against DNA oxidation: Results of human and animal experiments, *Mutat. Res.-Fund. Mol. M.*, 2011, **715**, 61–71.

35 M. Kundi, J. Bichler, M. Mišík and C. Hoelzl, Potent protection of gallic acid against DNA oxidation: Results of human and animal experiments, *Mutat. Res. Fundam. Mol. Mech. Mutagen.*, 2011, **715**, 61–71.

36 M. Arabi, M. Ghaedi and A. Ostovan, Synthesis and application of in-situ molecularly imprinted silica monolithic in pipette-tip solid-phase micro extraction for the separation and determination of gallic acid in orange juice samples, *J. Chromatogr. B*, 2017, **1048**, 102–110.

37 F. J. Benitez, F. J. Real, J. L. Acero, A. I. Leal and C. Garcia, Gallic acid degradation in aqueous solutions by UV/H2O2 treatment, Fenton's reagent and the photo-Fenton system, *J. Hazard Mater.*, 2005, **126**(1–3), 31–39.

38 X. Guan, S. Yan, Z. Xu and H. Fan, Gallic acid-conjugated iron oxide nanocomposite: An efficient, separable, and reusable adsorbent for remediation of Al (III)-contaminated tannery wastewater, *J. Environ. Chem. Eng.*, 2017, **5**(1), 479–487.

39 G. G. Celestino, R. R. Henriques, A. L. Shiguihara, V. R. Constantino and J. A. Júnior, Adsorption of gallic acid on nanoclay modified with poly(diallyldimethylammonium chloride), *Environ. Sci. Pollut. Res.*, 2019, **26**, 28444–28454.

40 Y. Zhang, P. He, L. Jia, T. Zhang, H. Liu, S. Wang and S. Zhou, Dimensionally stable Ti/SnO_2-RuO_2 composite electrode based highly efficient electrocatalytic degradation of industrial gallic acid effluent, *Chemosphere*, 2019, **224**, 707–715.

41 N. Majeed, N. Shah, A. Hameed, M. Shah, H. Gul, N. Ullah, T. Rehan, M. Elodemi, H. A. Ogaly, A. Khan and A. Al-Harrasi, Synthesis and characterization of multifunctional chitosan-grafted hydrogel for controlled drug delivery and electrochemical applications, *J. Drug Delivery Sci. Technol.*, 2025, **107**, 106770.

42 D. R. Mulinari and M. L. C. Silva, Adsorption of sulphate ions by modification of sugarcane bagasse cellulose, *Carbohydr. Polym.*, 2008, **74**, 617–620.

43 J. Shah, M. R. Jan, M. Khan and S. Amir, Removal and recovery of cadmium from aqueous solutions using magnetic nanoparticle-modified sawdust: kinetics and adsorption isotherm studies, *Desalination Water Treat.*, 2016, **57**, 9736–9744.

© 2026 The Author(s). Published by the Royal Society of Chemistry

Open Access Article. Published on 23 April 2026. Downloaded on 5/22/2026 8:14:12 PM. This article is licensed under a Creative Commons Attribution-NonCommercial 3.0 Unported Licence.

44 S. Hasan, A. Krishnaiah, T. K. Ghosh, D. S. Viswanath, V. M. Boddu and E. D. Smith, Adsorption of divalent cadmium Cd(II) from aqueous solutions onto chitosan-coated perlite beads, *Ind. Eng. Chem. Res.*, 2006, **45**, 5066–5077.

45 H. Khan, Iram, K. Gul, B. Ara, A. Khan, N. Ali, N. Ali and M. Bilal, Adsorptive removal of acrylic acid from the aqueous environment using raw and chemically modified alumina: Batch adsorption, kinetic, equilibrium and thermodynamic studies, *J. Environ. Chem. Eng.*, 2020, **8**, 103927.

46 J. Golveia, M. F. Santiago, L. B. Silva, L. C. Campos and F. Schimidt, Utilization of the corncob agro industrial residue as a potential adsorbent in the biosorption of bisphenol-A, *J. Braz. Chem. Soc.*, 2021, **32**, 1396–1404.

47 N. Ayawei, A. N. Ebelegi and D. Wankasi, Modelling and interpretation of adsorption isotherms, *J. Chem.*, 2017, **11**, 2017.

48 A. K. Agarwal, Kinetic behavior for the adsorption of different metal ions using fly ash, *J. Chem. Technol. Metall.*, 2021, **56**, 775–781.

49 T. Ullah, K. Gul, H. Khan, B. Ara and T. U. H. Zia, Efficient removal of selected fluoroquinolones from the aqueous environment using reduced magnetic graphene oxide/polyaniline composite, *Chemosphere*, 2022, **293**, 133452.

50 H. Khan, W. Ahmad, I. Hussain, M. Imran, M. S. Afridi and S. Ullah, Phytochemical composition, antioxidant and antimicrobial activities of leaves of *Olea europaea* wild variety, *J. Food Meas. Char.*, 2020, **14**, 640–648.

51 S. Alahyaribeik, S. D. Sharifi, F. Tabandeh, S. Honarbakhsh and S. Ghazanfari, Stability and cytotoxicity of DPPH inhibitory peptides derived from biodegradation of chicken feather, *Protein Expression Purif.*, 2021, **177**, 105748.

52 D. Yin, Y. Guo, M. Li, W. Wu, J. Tang, Y. Liu and F. Hu, Performance of VITEK 2, E-test, Kirby-Bauer disk diffusion and modified Kirby-Bauer disk diffusion compared to reference broth microdilution for testing tigecycline susceptibility of carbapenem-resistant *K. pneumoniae* and *A. baumannii* in a multicenter study in China, *Eur. J. Clin. Microbiol. Infect. Dis.*, 2021, **40**, 1149–1154.

53 R. Atchudan, T. N. J. I. Edison, S. Perumal, R. Vinodh, N. Muthuchamy and Y. R. Lee, One-pot synthesis of Fe_3O_4@graphite sheets as electrocatalyst for water electrolysis, *Fuel*, 2020, **277**, 118235.

54 X. Huang, J. Zhuang, D. Chen, H. Liu, F. Tang, X. Yan and J. Ren, General strategy for designing functionalized magnetic microspheres for different bioapplications, *Langmuir*, 2009, **25**, 11657–11663.

55 A. M. El-Nahas, T. A. Salaheldin, T. Zaki, H. H. El Maghrabi, A. M. Marie, S. M. Morsy and N. K. Allam, Functionalized cellulose-magnetite nanocomposite catalysts for efficient biodiesel production, *Chem. Eng. J.*, 2017, **322**, 167–180.

56 D. Shao, G. Hou, F. Chi, X. Lu and X. Ren, Transformation details of poly(acrylonitrile) to poly(amidoxime) during the amidoximation process, *RSC Adv.*, 2021, **11**, 1909–1915.

57 N. Priyadarshni, P. Nath and N. Chanda, Sustainable removal of arsenate, arsenite and bacterial contamination from water using biochar stabilized iron and copper oxide nanoparticles and associated mechanism of the remediation process, *J. Water Proc. Eng.*, 2020, **37**, 101495.

58 A. Azizi, Green synthesis of Fe_3O_4 nanoparticles and its application in preparation of Fe_3O_4/cellulose magnetic nanocomposites: A suitable proposal for drug delivery systems, *J. Inorg. Organomet. Polym. Mater.*, 2020, **30**, 3552–3561.

59 F. Osanlou, F. Nemati and S. Sabaqian, An eco-friendly and magnetized biopolymer cellulose-based heterogeneous acid catalyst for facile synthesis of functionalized pyrimido[4,5-b]quinolines and indeno fused pyrido[2,3-d]pyrimidines in water, *Res. Chem. Intermed.*, 2017, **43**, 2159–2174.

60 S. Chowdhury, R. Mishra, P. Saha and P. Kushwaha, Adsorption thermodynamics, kinetics and isosteric heat of adsorption of malachite green onto chemically modified rice husk, *Desalination*, 2011, **265**, 159–168.

61 N. Baylan, I. Ilalan and I. Inci, Copper oxide nanoparticles as a novel adsorbent for separation of acrylic acid from aqueous solution: Synthesis, characterization and application, *Water, Air, Soil Pollut.*, 2020, **231**, 465.